Containerless Liquid to Solid Nucleation Pathways in Two Representative Grades of Commercially Available Zirconium

Aaron J. Rulison* and Won-Kyu Rhim†
Jet Propulsion laboratory
Mail Code 183-401
4800 oak Grove Drive
Pasadena, California 91109

Robert Bayuzick, William Hofmeister, and Craig Morton
Vanderbilt University
Nashville, Tennessee 372.35

5/10/95

*NASA/NRC Resident Research Associate;
† to whom correspondence should be sent.

Abstract

Experimental measurements were conducted to determine the solid metal nucleation pathways of radiatively cooling, molten zirconium spheres of two different commercially available purity grades in a high-vacuum, high-temperature electrostatic levitator. The ensemble distribution of maximum undercooking temperatures was interpreted using Poisson statistics to determine the temperature dependence of the solid metal nucleation rate. For a sample of nominally 99.9590 pure zirconium, the results are consistent with heterogeneous solid metal nucleation either on static catalyst particles at least ~30 nm diameter or on a surface coating. For a sample of nominally 99% pure zirconium, however, it appears that heterogeneous solid metal nucleation occurred either on a polydispersion of ~10 nm (mean diameter) static catalyst particles or on dynamic catalyst particles which precipitated from a solution which became supersaturated as the melt cooled. A quantitative analysis of the compositions of both samples suggests that the catalysts probably consisted of one or more of the following elements: niobium, molybdenum, hafnium, and oxygen.

1.-. Introduction

Metallurgical processes which involve molten metals often depend on deep undercooking of the liquid. The depth of undercooling strongly influences the microstructure of solidified metals and alloys [1], thereby influencing the properties of the final product. Clearly, reliable guidelines are needed to predict the lifetimes and undercooking limits of metallic melts in order to calculate constraints on material purity and compositions and to design and optimize processes. The under-cooling limit in turn is governed by he solid metal nucleation rate.

The solid metal nucleation rate is affected by impurity particles when the foreign surfaces they present to the undercoo ed melt catalyze solidification. impurity particles which do not dissolve in the melt are called “static catalyst particles”, while impurity particles which dissolve at high temperatures and reappear as the melt

undercooks are called “dynamic catalyst particles” [2]. The potency of both static and dynamic catalyst particles increases with decreasing contact angle with the critical solid metal nucleus. in addition, the potency depends on the size of the catalyst particle relative to the critical solid metal nucleus (see the Appendix and Fig. Al). Catalyst particles which are at least one order of magnitude larger than the critical solid metal nucleus asymptotically approach a constant potency and may be called “fully active catalyst particles”; those that are at least one order of magnitude smaller than the critical solid metal nucleus have very low potency and may be called “inactive catalyst particles”; those whose size is of the order of critical solid metal nucleus may be called “transitional catalyst particle s.”

The potency of transitional catalyst particles increases rapidly as their size relative to the critical solid metal nucleus increases. The radius of the critical solid metal nucleus decreases approximately linearly with increasing undercooling. The potency of transitional catalyst particles, therefore, increases rapidly with increasing undercooking. The concept of an activation temperature for catalyst particles has long been accepted by cloud physicists concerned with the freezing of supercooled water droplets [3]. When the catalyst particles are monodisperse, the increasing potency will steepen the already abrupt increase in the solid metal nucleation rate with increasing undercooking. When tile catalyst particles are polydisperse, successively smaller sizes are activated as the melt cools, resulting in a more gradual increase in solid metal nucleation rate with increasing undercooking.

Both dynamic and static catalyst particles lead to an increased rate of heterogeneous solid metal nucleation as their amounts increase. (Fig. 1). Dynamic catalyst particles precipitate at a rate which depends on the concentration of dissolved impurities. Dynamic catalyst particles may precipitate on static catalyst particles (heterogeneous precipitation) or may precipitate homogeneously. If the dynamic catalyst particles precipitate on a time scale much longer than the time scale of homogeneous solid metal nucleation, the solid metal will nucleate homogeneously (Fig. 1, #1). If, however, the dynamic catalyst particles precipitate on a time scale much shorter

than the time scale of homogeneous solid metal nucleation, and if the new surfaces they form are highly potent catalysts, then heterogeneous solid metal nucleation will occur quickly after precipitation, i. e., $\Delta t_1 >> \Delta t_2$ in Fig. 1, #2. In that case the solid metal nucleation rate is approximately equal to the rate of precipitation of the soluble impurities. If the dynamic catalyst particles precipitate on a time scale much shorter than the time scale of homogeneous solid metal nucleation, and if the new surfaces they form are only mildly potent catalysts, then the melt is still governed by homogeneous solid metal nucleation (Fig. 1, #3). At sufficiently high number concentrations, however, even mildly potent dynamic catalyst particles will influence the solid metal nucleation rate (Fig. 1, #4). In case #4 the solid metal nucleation rate is affected by both the precipitation rate and subsequent heterogeneous solid metal nucleation rate.

A similar but less complicated scenario describes the solid metal nucleation rate in the case of static catalyst particles. If the rate of solid heterogeneous metal nucleation on static catalyst particles is low compared to the rate of homogeneous solid metal nucleation, then solidification is governed by the rate of homogeneous solid metal nucleation (Fig. 1, #5). In the case of highly potent static catalyst particles, the rate of heterogeneous solid metal nucleation will exceed the rate of homogeneous solid recta] nucleation, and solidification is governed by the rate of heterogeneous solid metal nucleation (Fig. 1, #6). Mildly potent static catalyst particles do not affect solid metal nucleation when present in low concentrations (Fig. 1, #7), but they set the solid metal nucleation rate if presence in sufficient amounts (Fig. 1, #8).

More complicated sequences of precipitation and nucleation events than those shown in Fig. 1 are possible. For example, both static and dynamic catalyst particles could be present in the same melt. Various compositions of dynamic catalyst particles could precipitate over a range of temperatures.

Solid metal nucleation was extensively studied by Turnbull, who demonstrated deep undercooking levels in small droplets of mercury, gallium, tin, bismuth, lead, antimony, aluminum, germanium, silver,

gold, copper, manganese, nickel, cobalt, iron, palladium, and water [4]. He went on to perform experiments on undercooled emulsified liquid mercury droplets with various coatings and showed that the results were consistent with classical homogeneous and heterogeneous nucleation theory [5]. Comparatively few studies have been performed on melts containing either static or dynamic catalyst particles. The precipitation of soluble impurities during undercooking was analyzed by Turpin and Elliot [6], who observed precipitated Fe-O-Si and Fe-O-Al particles in quenched iron melts. Libera et al. demonstrated the important role of dynamic catalyst particles in rapid solidification processing of atomized metal droplets [2].

The goal of this study was to explore the solid metal nucleation pathways for two representative grades of commercially available zirconium, a refractory metal. We begin with a discussion of classical nucleation theory, applied both to solidification of metals and to precipitation of soluble impurities. Then we discuss the experimental method for measuring the temperature-dependent solid metal nucleation rate. Finally, we discuss the measured solid metal nucleation rates and speculate on the presence of static and dynamic catalytic impurity particles and their effect on solid metal nucleation in these zirconium melts.

2. Analytical Prediction of Solid Metal Nucleation Rate

In this section we derive expressions for the rate of solid metal nucleation in the presence of transitional and fully active static catalyst particles (Fig. 1, #5, 6, 7, 8) and dynamic catalyst particles for the case where heterogeneous solid metal nucleation occurs quickly after precipitation (so-called "highly potent dynamic catalyst particles" in Fig. 1, #2). The results form a sufficient basis for discussion of the experimental results presented in Section 5.

2.1 Static Catalyst Particles (Fig. 1. #5 through #8)

The mathematical symbols in this section are listed in Table 1. In classical nucleation theory [7], solid clusters formed by random thermal fluctuations in an undercooked liquid are only stable above a

critical size which occurs at the cluster's maximum excess Gibbs free energy. The nucleation rate of stable solid clusters can be conceptualized as the number density of critical clusters multiplied by the arrival rate of single atoms to those clusters multiplied by a correction term. The number density of critical clusters is approximated by a Boltzmann distribution over cluster energy and is proportional to the number density of atoms in the liquid, N_1. The arrival rate of single atoms to those cluster is also proportional to N_1. Hence, the nucleation rate in classical nucleation theory is proportional to N_1^2. Similarly, if classical nucleation theory is applied to precipitation of impurities, the precipitation rate is proportional to N_p^2, where N_p is the number density of impurity atoms or molecules in the melt.

To elaborate, stable clusters of the solid form by random thermal motions of atoms at a rate given by

$$J_s = P_s \exp \frac{C_s(T)T^2}{\Delta T_s^2} \tag{1}$$

where the pre-exponential factor

$$P_s = N_1^2 K_s$$

$$= N_1^2 \left(\frac{\sigma_s}{kT}\right)^{1/2}\left(\frac{2v_s}{9\pi}\right)^{1/3} \frac{A_f A_s s_s^2}{V} \frac{kT}{h} \exp\left(\frac{-Q_s}{kT}\right) \tag{2}$$

The interracial surface energy σ_s can be estimated from the excess configurational entropy of the liquid relative to the solid [8, 9], i.e.,

$$\sigma_s = \frac{0.86\Delta S_s T}{N_{I.}^{1/3} V_M^{2/3}} \ . \tag{3}$$

Equation (3) predicts a linear dependence on temperature, but it has a zero intercept, which is not consistent with Turbull's results on liquid mercury [5]. Nevertheless, we use it here for lack of a more

reliable formula, and we analyze the effect of the temperature dependence of σ_s when interpreting the experimental results.

Equation (1) assumes that a steady-state rate of nucleation has been reached. The activation energy for liquid diffusion, Q_s, can be found for normal metals from the melting temperature through the empirical relation $Q_s = 10.5\,T_m^{1.15}$ J/mol, where T_m is in K [10] . The exponential factor in Eq. (1) is

$$C_s(T) = -\frac{16\pi\sigma_s^3 T_m^2 f_s(T)}{3T^3 H_s^2 k}, \qquad (4)$$

where the catalytic potency factor, $f_s(T)$, accounts for the fact that it is energetically easier for a cluster to form on a foreign surface than to form independently. For fully active catalyst particles (much larger than the critical solid metal nucleus), $C_s(T) \approx const.$ because σ_s - T and $f_s \approx const.$ For a monodisperi sion of transitional catalyst particles, $f_s(T)$ increases rapidly with decreasing T [11, 12]. For a polydispersion of transitional catalyst particles, the average fs(T) increases gradually with decreasing T as particles of successively smaller sizes in the distribution are activated.

2.1 Highly P e t ent Dynamic Catalyst Particles (Fig. 1, #2)

If classical nucleation theory can be used to describe the precipitation of soluble impurities, the precipitation rate has a form identical to Eq. (l). The precipitation is driven by the Gibbs free energy difference between dissolved impurities and their precipitates and may occur on pre-existing catalytic particles; that is, catalytic particles of one composition may grow on particles of another composition. Soluble impurities could be introduced through chemical reactions with residual gases in the chamber or may originate in the metal stock. According to the theory, the precipitation rate of impurity particles with spherical surfaces on pre-existing catalyst particles is

$$J_p = P_p \exp \frac{C_p T^2}{\Delta T_p^2} \tag{5}$$

where the pre-exponential factor

$$P_p = N_p^2 K_p$$

$$= N_p^2 \left(\frac{\sigma_p}{kT}\right)^{1/2} \left(\frac{2v_p}{9\pi}\right)^{1/3} \frac{A_f A_p s_p^2}{V} \frac{kT}{h} \exp\left(\frac{-Q_p}{kT}\right) \tag{6}$$

Equation (5) assumes that a steady-state rate of precipitation has been reached. The exponential factor in Eq. (5) is

$$C_p(T) = -\frac{16n:p3Tcq:fE(\sim)}{3T^3 kH_p^2} \quad \text{“} \tag{7}$$

For heterogeneous precipitation of dynamic catalyst particles on fully active catalyst particles (much larger than the critical solid metal nucleus), $C_p(T) \approx const.$ because σ_p - '1' and $f_p \approx const.$ As was the case in solid metal nucleation, for a monodispersion of transitional catalyst particles, $f_p(T)$ increases rapidly with decreasing T [11, 12]. For a polydispersion of transitional catalyst particles, the average $f_p(T)$ increases gradually with decreasing T as particles of successively smaller sizes are activated.

It is important to note that $N_p/N_1 << 1$ due to the dilution of impurities. Furthermore, K_p should not differ from K_s by more than two or three orders of magnitude. Therefore, the ratio of the pre-exponential factors given by Eels. (2) and (6) should satisfy the following relationship:

$$\frac{P_p}{P_s} = \frac{K_p}{K_s} \frac{N_p^2}{N_1^2} << 1. \tag{8}$$

Two important results from the above analysis bear repeating. First, the pre-exponential factor in the rate of precipitation of dynamic catalyst particles should be many orders of magnitude less than the pre-exponential factor in the rate of nucleation of solid metal. Second, the pre-exponential factors are affected by the size distribution of transitional catalyst particles; wider spreads in the size distribution result in lower pre-exponential factors.

3. Experiment

In order to eliminate the catalysis of solid metal nucleation caused by contact between the undercooked liquid and crucible surfaces, the samples were melted and solidified using the high-temperature high-vacuum electrostatic levitator (HTHVESL) at the Jet Propulsion Laboratory. The HTHVESL, described in detail elsewhere [13], utilizes an electric field to impart a counter-gravitational force on electrically charged, 2 to 3 mm diameter samples. Vacuum pressure is typically in the 10^{-8} to 10^{-6} Torr range. Samples can be heated to a maximum of about 2300 K using a 1 kW xenon arc lamp. The sample temperature is measured with a single color silicon pyrometer operating at **659** nm.

Two different zirconium samples were used in the present experiments. Zr#1 (40.6 mg) was of 99.95% nominal purity and was obtained from Teledyne Wah-Chang, Albany, Oregon, and prepared by arc-melting in an argon atmosphere on a water-cooled copper plate to form it into an approximate sphere. Zr#2 (39.1 mg) was of 99% nominal purity and was fabricated at JPL by electron beam melting the end of the rod obtained from Johnson Matthey, Ward Hill, MA, to form a pendant drop in a 10^{-7} Torr vacuum, which was allowed to solidify in vacuum and clipped off. The actual impurity compositions of each of the two samples will be discussed in the Results and Discussion section.

An undercooking run is performed by heating the sample at least $\approx$10 K above its melting point (Fig. 1, #1) and blocking the lamp to allow the sample to cool into the undercooled region (Fig. 1, #2 to #3). The cooling is purely radiative because of the low chamber pressure. A stable solid metal nucleus forms at the undercooking

temperature T_u (Fig. 1, #3) and quickly grows to engulf the entire sample, releasing the latent heat of fusion to form a mixture of liquid and solid at T_m (Fig. 1, #4). The sample remains at T_m until it completely solidifies (Fig. 1, #5) and then cools again (Fig. 1, #5 to #6). Undercooking runs can easily be repeated about twice per minute by controlling the heating lamp power. The chamber pressure, overheating temperature, and undercooking temperature are recorded for each run.

4. Derivation of the Solid Metal Nucleation Rate from Undercooking Limit Data

Scatter in the recorded values of undercooking limit within a series of undercooking experiments is caused in part by measurement errors. Even if noiseless measurements could be made, however, the undercooling limit would still show variations caused by the random nature of thermal motions leading to critical cluster formation. Each undercooking run is independent of the others, yet there is some average undercooling limit which becomes apparent after many measurements. This is the prescription for Poisson statistics. In zirconium undercooked to around $T = 0.85\ T_m$, the first stable solid metal nucleus grows so rapidly that only one stable nucleus is required to convert the entire sample to a solid. Therefore, we need an expression for the probability of formation of at least one stable nucleus after time t, which is

$$F(t) = 1 - \exp\left[-\int_0^t \mu(t')dt' \right] \qquad (9)$$

where μ is the rate of events which may be a function of time [14]. In undercooking experiments μ is either the specific solid metal nucleation rate or the specific precipitation rate integrated over the sample mass.

In the present experiments the sample cooled radiatively. Its surface temperature was about 3 K below the core temperature according to numerical calculations. Since the nucleation rate per

unit volume is a very sensitive function of temperature, it must be integrated over the sample's volume to determine the nucleation rate in the entire sample. In order to simplify the expressions that follow, we define an effective sample volume V_{eff} to account for the temperature gradient such that the nucleation rate evaluated at the sample's surface temperature multiplied by V_{eff} equals the temperature-dependent nucleation rate integrated over the actual sample. Using the numerically-calculated temperature gradient and integrating over the sample shows that $V_{eff} \approx$ O. IV, where V is the sample's actual volume. Then, using the transformation T = T(t), we obtain

$$F(T) = 1 - \exp\left[- \int_{T_l}^{T} V_{eff} J(T) \frac{dt}{dT} dT \right] \qquad (10)$$

where F(T) is the probability that at least one stable nucleus forms as the sample cools from T_l o T; T_l is equal to T_m for solid metal nucleation or T_{eq} for dynamic catalyst particle precipitation. We proceed by neglecting the time lag of nucleation. This approximation is not expected to affect the present results substantially and allows J(T) to be replaced by the steady-state solid metal nucleation rate, $J_s(T)$, or the steady-state dynamic catalyst particle precipitation rate, $J_p(T)$. In the present experiments the undercooling runs taken together form an ensemble set of data so F(T) is the normalized cumulative distribution of recalescence events taken from the set of measured undercooking temperatures.

A comparison of the measured F(T) to that expressed by Eq. (10) can be obtained by making mathematical approximations to allow an analytical solution to the integral [15]. Realizing that the dependence on temperature of the exponential term in the nucleation rate is much stronger than the pre-exponential term, Eq. (10) becomes (after algebraic manipulations and approximations)

$$\ln \ln \frac{1}{1-F(T)} \approx \ln \left| \frac{PV_{eff} \frac{dt}{dT}}{\frac{d}{dT}\left(\frac{C(T)T^2}{\Delta T^2}\right)} \right|_{T^*} + \frac{C(T)T^2}{\Delta T^2} \qquad (11)$$

where P is P_s for solid metal nucleation or P_p for dynamic catalyst particle precipitation, C(T) is $C_s(T)$ for solid metal nucleation or $C_p(T)$ for dynamic catalyst particle precipitation, T* is chosen to be the average undercooking limit temperature, and AT is ΔT_s for solid metal nucleation or ΔT_p for dynamic catalyst particle precipitation. For the case of fully active catalyst particles we have $C \approx const.$ and Eq. (11) simplifies to

$$\ln \ln \frac{1}{1-F(T)} \approx \ln \left(\frac{PV_{eff} \frac{dt}{dT} \Delta T^3}{2C \; 2C \; TT_1} \right)_{T^*} + C \frac{T^2}{\Delta T^2}, \qquad (12)$$

Equation (12) shows that a plot of the experimental data as $\ln \ln \frac{1}{1-F(T)}$ versus $\frac{T^2}{\Delta T^2}$--- should result in a straight line with slope C and intercept

$$M = \ln \left(\frac{PV_{eff} \frac{dt}{dT} \Delta T^3}{2C \; TT_1} \right)_{T^*} . \qquad (13)$$

Equation (11) is quite sensitive to the temperature dependence of σ. The effects of the temperature dependence of σ will be considered when interpreting the experimental results.

The results will also be affected by measurement errors because any scatter in the data widens the range of measured temperatures. Measurement error ultimately decreases the calculated values of the intercept, M, and magnitude of the slope, ICI. Even a slight change in slope drastically affects the calculated value of the intercept. For example, a 10% increase in ICI for the low pressure Zr#1 data results

in two orders of magnitude increase in M. Thus the. values of M and ICI reported below are lower bounds to the true values. The pyrometer and associated data reduction used to calculate temperature are estimated to exhibit a standard deviation of about 4 K. Since the range of maximum undercooking temperatures in an ensemble of about 100 experiments only spans about 20 K, the measurement error of 4 K must add substantially to the natural variation. A quantitative analysis aimed at accounting for the pyrometer noise could be attempted but would require accurate statistical data on the noise itself. Instead, this paper will focus on qualitative trends in the data.

5. Results and Discussion

5.1 solid Metal Nucleation Frequencies

The undercooking temperatures obtained for Zr#1 and Zr#2 are plotted against chamber pressure in Fig. 2. Zr#1 undercooked an average of 15.5%, independent of pressure, while Zr#2 undercooked an average of only 14 .2%, independent of pressure. The measured undercoolings indicate that the radius of the critical solid zirconium nucleus, given by $\frac{2\sigma_s T}{H_S \Delta T_s}$, ranged from about 2.9 nm to 2.4 nm at 280 K and 335 K undercooking, respectively.

Figure 3 shows that the undercooking was not a function of overheating for Zr#1. Overheating data was not available for Zr#2. The lack of dependence of undercooking on overheating allows more convenient experimentation since the overheating temperature need not be controlled as long as it falls within the range shown in Fig. 3. Furthermore, the lack of dependence of undercooking on overheating implies that any long-range order in the liquid is destroyed when it is heated sufficiently above its melting temperature [16, 17]. The results shown in Fig. 3 indicate that overheating $\approx$10 K was sufficient to ensure no long-range order in molten zirconium. The lower limit of overheating required to ensure no long-range order may be less than $\approx$10 K but measurements below that value were not attempted.

Figure 4 shows the normalized cumulative distribution of solid metal nucleation events versus temperature, F(T), for Zr#1 and Zr#2. The same data is plotted as in $\ln \frac{1}{1-F(T)}$ versus $\frac{T^2}{\Delta T_s^2}$ in Fig. S. The data fits straight lines with slopes and intercepts given in Table 2. The fact that the data falls on straight lines contrasts with the results obtained in electromagnetic levitators and drop tubes [15]. Apparently, the experimental conditions afforded by the high-temperature high-vacuum electrostatic levitator eliminate premature solidification and allow solid metal nucleation and/or dynamic catalyst particle precipitation to control undercooking. The data quality, however, is not sufficient to make a definitive test of classical nucleation theory. Nevertheless, the data indicates which major pathways led to solid zirconium nucleation in these melts containing realistic impurity levels.

The measured solid metal nucleation rate of Zr#1 and Zr#2 are found from the slope and intercept in Fig. 5 as described in Section 4. The result for Zr#1 is

$$J(T) \approx 1029 \exp\left[-1.47\frac{T^2}{(T_m - T)^2}\right] \quad m^{-3}s^{-1} \tag{14}$$

The result for Zr#2 is

$$J(T) \approx 10^{19} \exp\left[-0.574\frac{T^2}{(T_m - T)^2}\right] \quad m^{-3}s^{-1}. \tag{15}$$

For Zr#1, the experimentally-observed nucleation rate ranged from 5 to 280 nuclei/s, as calculated by inserting the experimentally-measured lowest and highest maximum undercooking temperatures in Eqn. (14). For Zr#2, the experimentally-observed nucleation rate ranged from 2 to 290 nuclei/s. The range would be widened if more undercooking runs were performed.

Note that the exponential factor for Zr#1 is about 2.6 times that of Zr#2 and the pm-exponential factor for Zr# 1 is 10 orders of

magnitude greater than that of Zr#2. Recall that Zr#1 was nominally 99.95% pure while Zr#2 was nominally 99% pure. The actual impurity levels are quantified below. On the basis of these results we can say with certainty that *the impurity concentration had a very strong effect on the solid metal nucleation rate.* This is clear despite the fact that the average maximum undercooking temperatures for Zr#1 and Zr#2 agree to within 10%.

5.2. The Effect of Impurities on Solid Metal nucleation

In this section we speculate on possible causes for such marked sensitivity of the solid metal nucleation rate on sample purity. First, consider the role of surface reactions. Nucleation of solid zirconium could conceivably be catalyzed on impurities which form through chemical reactions with vacuum chamber residual gases. Those gases primarily consist of water vapor, oxygen, and hydrogen, the total pressure of which was about 10^{-7} to 10^{-6} Torr. However, it is difficult to explain how the small difference in impurity concentration between Zr#1 and Zr#2 could affect surface reactions enough to so drastically alter the solid metal nucleation rate. Therefore, let us examine solid metal nucleation as it might occur throughout the bulk of the sample rather than on the surface.

In. the present experiments, the undercooking limit is marked by recalescence of the sample, which occurs only after nucleation of solid zirconium. If recalescence is the final result of a single-step process such as nucleation of solid zirconium on static catalyst particles (Fig. 1, #6 or #8), then the statistics of the undercooking will reflect that single step. If, however, recalescence is the final result of a two-step process wherein nucleation of solid zirconium occurs only after precipitation of dynamic impurity particles (Fig. 1, #2 or #4), then the statistics of the undercooking will reflect the rate-limiting step, which could be either solid metal nucleation or dynamic catalyst particle precipitation.

Of course, it is not known a *priori* whether undercooking was governed by direct nucleation of solid zirconium or precipitation of dynamic catalyst particles upon which solid zirconium nucleated. If nucleation of solid zirconium is the rate-limiting step, then the pre-

exponential factor should correspond to Eq. (2), while if precipitation is the rate-limiting, step, the pre-exponential factor should correspond to Eq. (6). Recall that, as shown in Eq. (8), the value of the pre-exponential factor, P_p, for dynamic catalyst particle precipitation is lower than that for solid metal nucleation, Ps, by a factor X^2, where X is the mole fraction of the precipitating impurity, ignoring smaller order factors. For example, if $X - 10^{-5}$ (10 ppm), then $P_p/P_S - 10^{-10}$. On the other hand, the size distribution of catalyst particles also affects the pre-exponential factor. Catalyst particles make the transition from inactive to fully active catalysts as the radius of the solid metal nucleus decreases with increasing undercooking. The transition of a population of catalyst particles to the fully active state occurs gradually when the distribution of sizes is wide. Therefore, for a wide size distribution of catalysts particles with mean size ~1 nm, the solid metal nucleation rate is boosted gradually with increasing undercooking. A gradual increase in solid metal nucleation rate corresponds to a low pre-exponential factor.

Consider again the observed solid metal nucleation rate of Zr#1 given in Eq. (14). If undercooling was limited by catalyzed nucleation of solid zirconium on fully active static catalyst particles (larger than about 30 nm diameter), then Eqs.(1) through (4) apply with $C_s \approx const.$ Equation (2) gives $A_f = 10^{-12}\ m^2$, which is reasonable; for example, 10^3 particles 10 nm in diameter evenly dispersed throughout the sample could account for the observed values of A_f. Or, if we assume $\sigma = const.$ rather than linearly proportional to T, then A_f is computed to be about $10^{-6}\ m^2$, which is also reasonable. Thus, for Zr#1 sample data, it is possible that nucleation of solid zirconium occurred on fully active static catalytic particles or perhaps an insoluble coating on the sample's surface. Equation (4) shows that the potency factor, fs, for this process would be about 0.17.

If it is assumed that undercooking of Zr#2 was governed by solid metal nucleation on fully active static catalyst particles as assumed for Zr#1, then we obtain $A_f = 10^{-22}\ m^2$ if σ is assumed to be linearly proportional to T or $10^{-16}\ m^2$ if σ is assumed to be constant.

These values of A_f are far below realistic surface areas. In light of Eq. (8), it may be more reasonable to assume that precipitation of impurity particles occurred as a rate-limiting step, after which solid zirconium heterogeneously nucleated as depicted in Fig. 1, #2. On the other hand, a polydispersion of -1 nm static catalyst particles might also account for the low pre-exponential factor.

To determine the parameters of precipitation, such as P_p, the data would have to be plotted using in in I/(1-F) vs. $T^2/\Delta T_p^2$ rather than vs. $T^2/\Delta T_s^2$. At this time, however, the compositions of impurities are known (see below) but the composition of precipitates and the reactions governing precipitation are not, so ΔT_p, and hence P_p, cannot be found. It is clear, however, that the static catalyst particle scenario is not supported by the observed nucleation rate of solid zirconium in Zr#2.

Compositional analyses were performed on Zr#1 and Zr#2 to identify which impurity elements were present. Glow discharge mass spectrometry was performed on the spheres after the undercooking experiments by Shiva Technologies, Inc., Cicero, New York. Table 3 shows the molar concentrations of elements in parts per million. The sample holder used in the measurements was tantalum so its concentration in the samples could not be measured. Table 3 shows that Zr#2 contained 830 ppm of oxygen while Zr#1 contained only 390 ppm. Zr#2 also contained substantially more C, N, F, S, Ti, Nb, Mo, and Hf than Zr#1. Zr#2 contained substantially less Si, U, and W than Zr#1. For Zr#1, we speculate that insoluble impurities (at least -30 nm in diameter) consisting of silicon carbide and tungsten carbide may have been responsible for catalyzing solid metal nucleation. The quantity of those elements was more than sufficient to account for the observed catalytic surface area. As for Zr#2, we speculate that in addition to silicon carbide and tungsten carbide static catalyst particles, dynamic catalysts particles (perhaps consisting of combinations of Hf, Nb, and Mo with O) precipitated and subsequently catalyzed nucleation of solid zirconium. Other precipitates are certainly possible. but an exhaustive list will not be

given here. Rather, a more detailed study of the role of soluble impurities will be left for future work.

7. conclusions

Two representative grades of commercially available zirconium were melted, undercooked, and solidified using a high temperature, high vacuum electrostatic levitator. The cumulative distribution of the maximum undercooking temperatures reached during radiative cooling were interpreted using an analysis based on Poisson statistics in order to determine the temperature dependence of the solid metal nucleation rate. The impurity concentration had a strong effect on the solid metal nucleation rate. We speculate that the present results may be explained by invoking a separate solid metal nucleation pathway for each sample. That is, the results are understandable if, for Zr#l, recalescence was the final result of a single-step process wherein nucleation of solid zirconium occurred on static catalyst particles (of diameter -30 nm or greater), or on a surface coating. For Zr#2, recalescence was either the result of (1) a two-step process wherein nucleation of solid zirconium occurred only after a relatively slow precipitation of dynamic catalyst particles or (2) heterogeneous solid metal nucleation on a polydisperse population of -1 nm diameter static catalyst particles.

Acknowledgments

AJR and WKR would like to thank Dr. Paul Wagner for computing the radial temperature profiles of radiatively-cooling zirconium spheres, and Mr. Kelly Perry for developing software for data analysis. This work was carried out at the Jet Propulsion Laboratory, under contract with the National Aeronautics and Space Administration. The Vanderbilt authors were supported by NASA grant #NAG8978 from the Microgravity Science and Applications Division.

Appendix: Values of f and A* in Catalyzed Nucleation and Precipitation

Derivations by Fletcher [11, 12] show that the Gibbs free energy required to form a spherical critical cluster on a catalytic surface is less than that required to form a critical cluster independently. The Gibbs free energy is reduced by a factor f which relates to the radius of curvature, R, of a spherical catalytic surface and the contact angle θ between the solid cluster and the catalytic surface measured through the solid. The relation is

$$f = \frac{1}{2} + \frac{1}{2}\left(\frac{1-mx}{g}\right)^3 + \frac{x^3}{2}\left\{2 - \frac{3(x-m)}{g} + \left(\frac{x-m}{g}\right)^3\right| + \frac{3mx^2}{2}\left(\frac{x-m}{g} - 1\right) \quad (A1)$$

where $g = (1 + X^2 - 2mx)^{1/2}$, $x = R/R_c$, R_c is the radius of curvature of the liquid/cluster interface, which is equal to $2\sigma T_s/H_s\Delta T_s$ for solidification or $2\sigma_p T_{eq}/H_p\Delta T_p$ for precipitation, and $m = \cos\theta$. See Fig. Al for a plot of Eq. (Al). The area of the critical cluster exposed to surrounding liquid is

$$A_c = 2\pi R_c^2[1 + (R_c - Rm)/d] \quad (A2)$$

where

$$d = (R^2 + R_c^2 - 2R_cRm)^{1/2}. \quad (A')$$

References

1. Spaepen, F. 1987. *Science, 235,* 1010-1014.

2. Libera, M., Olson, G. B., and Vander Sande, J. B. 1991. *Materials Science and Engineering, A132, 10"/ -118.* Equation(3) in this reference *is* incorrect. See Fletcher, N. H. 1963, *J. of Chemical Physics,* **38(1), 237-240.**

3. Bardsley, W. E., and Khatep, M. M. 1984. *J. of the Atmospheric Sciences,* **41(5), 856-862.**

4. Turnbull, D. 1950. *J. of Applied Physics, 21, 1022-1028.*

5. Turnbull, D. 1952. *J. of Chemical Physics 20(3), 411-424.*

6. Turpin, M. L., and Elliot, J. F. 1966. *J. Iron Steel Inst., 204, 217-225.*

7. Turnbull, D. 1949. *J. of Chemical Physics 17(1), 71-73.* Note erratum printed on page 429.

8. Spaepen, F. 1975. *Acts Metallurgic 23, 729-743.*

9. Herlach, D. M. 1991. *Annual Review of Materials Science 21,* 23-44.

10. Iida, T., and Guthrie, R. 1. L., 1988. The Physical Properties of Liquid Metals, Clarendon Press, Oxford.

11. Fletcher, N. H. 1958. The *Journal of Chemical Physics, 29(3), 572-576. See* erratum printed in 1959, *The Journal of Chemical Physics, 31, 1136.*

12. Fletcher, N. H. 1963. *The Journal of Chemical Physics, 38(1), 237-240.*

13. Rhim, W. K., Chung, S. K., Barber, D., Man, K. F., Gutt, G., Rulison, A. J., and, Spjut, R. E. 1993. *Review of Scientific Instruments 64(1 O), 2961-2970.*

14. Sridharan, R., and De Levie, R. 1984. *J. Elect roanalytical Chemistry* **169, 59-67.**

15. Morton, C. W., Hofmeister, W. H., Bayuzick, R. J., and Robinson, M. B. 1993. *Materials Science and Engineering A, 178, 209-215.*

16. Mühlberg, M., Rudolph, P., and Laasch, M. 1993, *Journal of Crystal Growth 128, 571-575.*

17. Glazov, V. M., Chizhevskaya, S. N., and Glagoleva, N. N. 1969. Liquid Semiconductors, Plenum Press, New York. See chapter 3, section 5.

18. Bonnell, Ph.D. Thesis, Rice University 1972.

19. Weast, R. C., and Astle, M. J., Eds. 1981. CRC Handbook of Chemistry and Physics, 62nd edition (CRC Press, Boca Raton, Florida).

20. Rulison, A. J., and Rhim, W. K. 1994, *Review of Scientific Instruments 65(3), 695-700.*

Table 1. Section 2 symbols in order of appearance.

N_1	number density of liquid Zr atoms
$'_P$	number density of impurity atoms or molecules in the met!
J_s	solid metal nucleation rate (events per unit time per unit volume)
P_s	pre-exponential fader in the classical solid metal nucleation rate
C_s	exponential factor in the classical solid metal nucleation rate
T	absolute temperature
ΔT_s	Tin-T
T_m	melting temperature
K_s	see text
σ_s	interracial surface energy between solid and liquid Zr
k	Boltzmann constant
v_s	volume of one atom of solid Zr
A_f	total surface area of static catalytic particles
A_s	area of a solid critical cluster of zirconium exposed to the surrounding liquid
s_s	jumping distance of a Zr atom in the met!
V	sample volume
h	Planck's constant
Q_s	activation energy for diffusion of Zr in liquid Zr
ASs	molar entropy of fusion of solid Zr
$'_L$	Avagadro's number
$'_M$	molar volume of solid Zr
f_s	catalytic potency factor for nucleation of solid metal on a catalytic surface
Hs	enthalpy of fusion of Zr
$'_P$	impurity precipitation rate (events per unit time per unit volume)
$'_P$	pre-exponential factor in the classical precipitation rate
C_p	exponential factor in the classical precipitation rate
ΔT_p	T_{eq} - T
T_{eq}	the temperature at which an impurity at a given concentration is saturated in the melt
$'_P$	see text
σ_p	interracial surface energy between the impurity precipitate and liquid zirconium
$'_P$	volume of one atom of precipitate
$'_P$	area of a precipitate particle exposed to the surrounding liquid
S_p	jumping distance of a impurity atom or molecule in the melt
$'_P$	activation energy for diffusion of impurity atoms or molecules in liquid Zr
f_p	catalytic potency factor for precipitation of impurities on a catalytic surface
$'_P$	enthalpy of dissolution

	Zr#1	Zr#2	units
c	< -1.47	≤ -0.574	dimensionless
M	> 43.2	≥ 20.5	dimensionless
$\sigma^3 f$	>1.3X10-3	> 5.0X10-4	$N^3 m^{-3}$
f_s	≥ 0.17	--	dimensionless
P	≥ 10^{29}	≥ 10^{19}	$m^{-3} s^{-1}$

Table 2. Results of fitting the experimental data to the classical solid metal nucleation theory.

T_m	2128 K
H_s	8.99×10^8 J/m^3
ρ_{liquid}	5600 kg/m^3
M	
$\varepsilon_{Tl,av}$	*0.28*
$c_{pl,av}$	447 J/kg K
ΔS_s	6.89 J/mole/K
V_M	1.63x 10-5 m^3/mol
v	2.43x 10-29 m^3
Q_s	1.17 X10-19 J/atom

Table 4. Properties of zirconium samples (H_s: [18]; ρ_{liquid}: [19]; $c_{pl,av}$ and $\varepsilon_{Tl,av}$: [20]; Q_s: from empirical relation for self-diffusion activation energy given in [10]; AS_s is approximated by H_s/T_m. This approximation is accurate if the configurational entropy is much greater than the vibrational entropy.)

Table 3. Concentration of impurities in Zr#1 and Zr#2 (molar basis, parts per million).

element	Zr#1	Zr#2	element	Zr#1	Zr#2
Li	<,66	<.66	Pd	<.0086	<.0086
Be	<.10	<.10	Ag	<.042	<.042
B	.34	.51	Cd	<.081	<.081
c	540	730	‘ i n	<.040	<.040
N	25	38	‘ S n	<.078	<.077
0	390	830	Sb	<.0075	<.0075
F	5.7	37	I-e	<.o36	<.036
Na	14	13	I	<.o36	<.036
Mg	<.19	<.19	‘ C s	<.0069	<.0069
Al	2.4	3.0	Ba	<.033	<.033
Si	240	78	‘ l a	<.033	<.033
P	<.29	<.29	Ce	<.0065	<,0065
s	2.60	140	Pr	<.0065	<.0065
Cl	<.13	<.13	Nd	<.0063	<.0063
K	<1.2	<1.2	Sm	<.0061	<.0061
Ca	<.23	<.23	Eu	<.oO6	<.0060
Sc	<10	<lo	Gd	<.0058	<.0058
Ti	<.05	1.1	Tb	<.0057	<.0057
V	<.018	<.018	Dy	<,0056	<.0056
Cr	<.088	<.09	Ho	<.0055	<.0055
MI	<.017	<.017	‘ E r	<.0055	<.0055
Fe	<.16	<.16	Tm	<.0054	<.0054
co	<.31	<.31	Yb	<.0053	<.0053
Ni	. 7 8	2.8	‘ L u	<.0052	<.0052
Cu	<1.4	<1.4	—H f	43	570
Zn	<.70	<.70	Ta	holder	holder
Ga	<.65	<.65	W	94	13
Ge	<.13	<.13	Re	<.0049	<.0049
As	<.061	<.061	Os	<.0048	<.0048
Se	<.12	<.12	I r	<.024	<.024
Br	<.057	<.057	Pt	<.047	<.047
Rb	<.053	<.053	Au	<.23	<.23
Sr	<.052	<.052	Hg	<.022	<.022
Y	C.10	<.10	TI	<.022	<.022
Zr	matrix	matrix	Pb	<.022	<.022
Nb	<.98	44	Bi	<.022	<.022
Mo	<.48	40	Th	<.0004	.0007
Ru	<.045	<.045	u	. 1 3	.0077
Rh	<.0089	<.0089			

Figure Captions

1. Dynamic catalyst particle precipitation and solid metal nucleation phenomena in impure undercooked melts. Higher concentrations of more potent catalyst materials (either static or dynamic) prevent homogeneous solid metal nucleation from governing the limit of undercooking. See the text for explanation of cases #1 through #8.

2. Temperature vs. time profile for a 40.7 mg spherical zirconium sample undergoing radiative cooling. The heat source was extinguished at #1. The sample reached its equilibrium melting temperature T_m = 2128 K at #2 and continued to cool into the undercooked region until recalescence occurred at #3, raising the sample's temperature back to T_m at #4. The sample maintained T_m until it completely solidified *(#5)* and then cooled as a solid.

3. Percentage of undercooking versus chamber pressure for Zr#1 and Zr#2. Undercooking averaged 15.5'% for Zr#1 and 14.2% for Zr#2 and did not depend on pressure (for either sample) in the ranges tested.

4. Percentage of undercooking versus percentage of overheating for Zr# 1. Undercooking averaged 15.5% and did not depend on overheating in the range tested.

5. Normalized cumulative probability of solid metal nucleation distributions for Zr#1 and Zr#2.

6. Normalized cumulative probability of solid metal nucleation distributions for Zr#1 and Zr#2 plotted as prescribed by the classical theory of heterogeneous solid metal nucleation on static catalyst particles. The slope of each straight line is the exponential factor while the intercept determines the pre-exponential factor through Eq. (13).

A1. Catalytic potency factor f vs. the ratio of catalytic particle radius R to critical solid nucleus radius R_c for various contant angles.

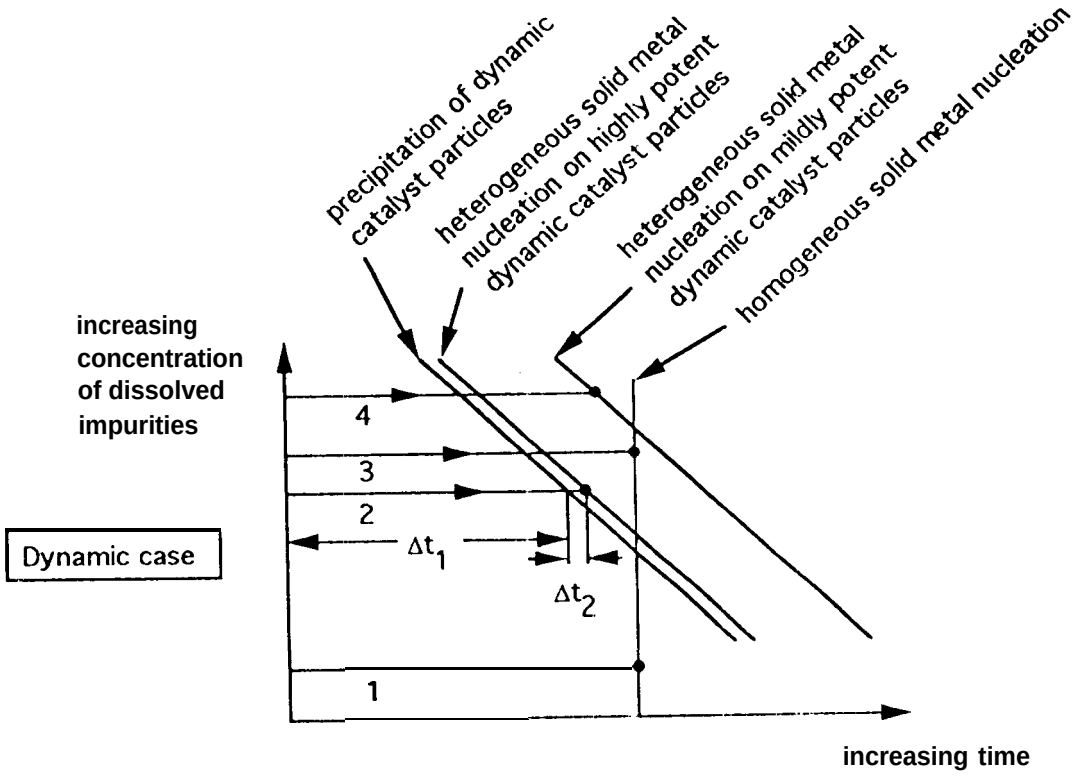
precipitation of dynamic catalyst particles
heterogeneous solid metal nucleation on highly potent dynamic catalyst particles
heterogeneous solid metal nucleation on mildly potent dynamic catalyst particles
homogeneous solid metal nucleation
increasing concentration of dissolved impurities
Dynamic case
4
3
2
1
Δt_1
Δt_2
increasing time

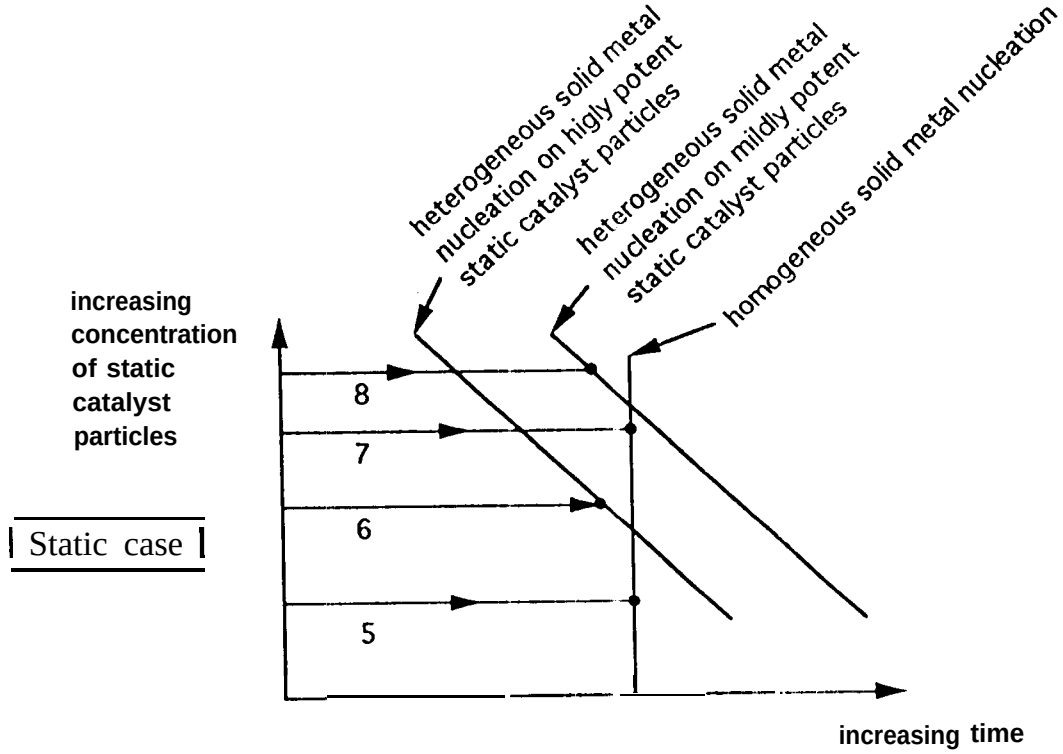
heterogeneous solid metal nucleation on higly potent static catalyst particles
heterogeneous solid metal nucleation on mildly potent static catalyst particles
homogeneous solid metal nucleation
increasing concentration of static catalyst particles
Static case
8
7
6
5
increasing time

Fig. 1.

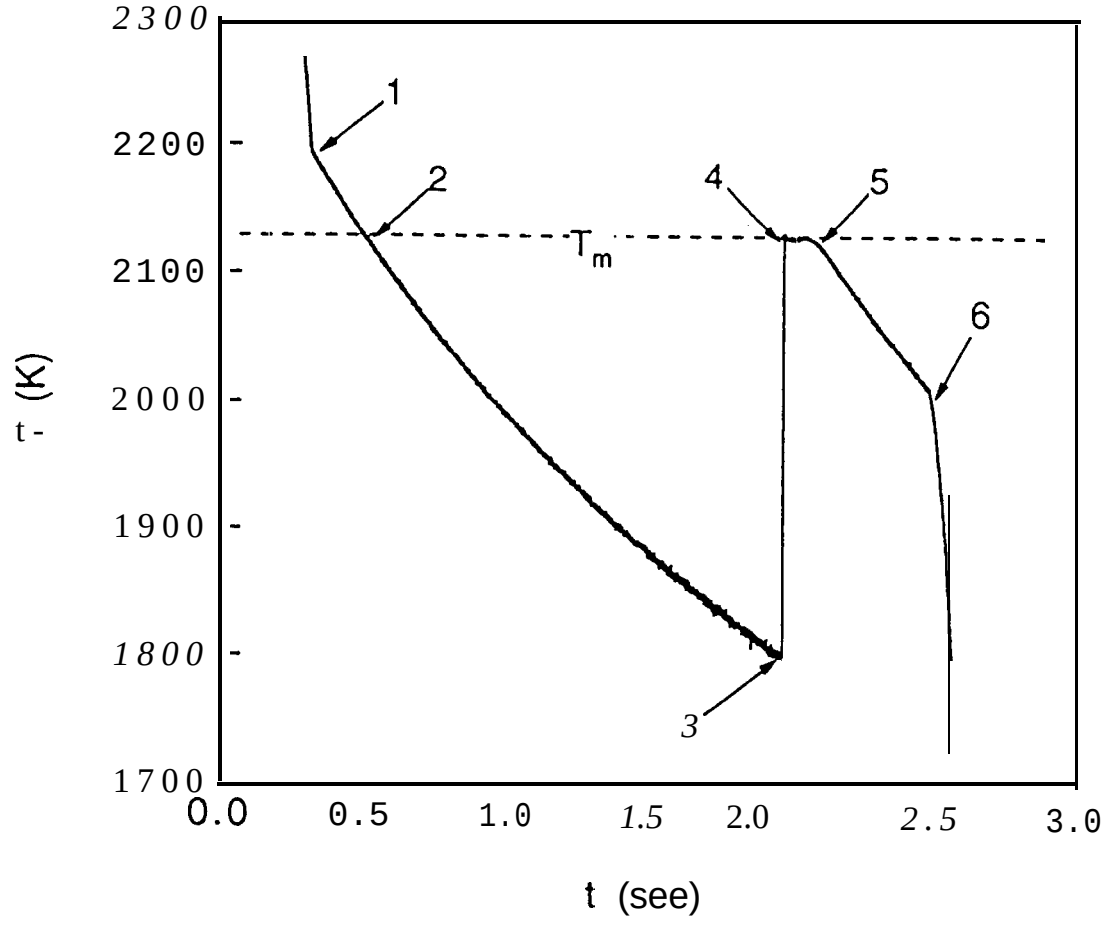
2300
2200
2100
2000
1900
1800
1700
t - (K)
0.0
0.5
1.0
1.5
2.0
2.5
3.0
t (see)
1
2
3
4
5
6
T_m

Fig. 2

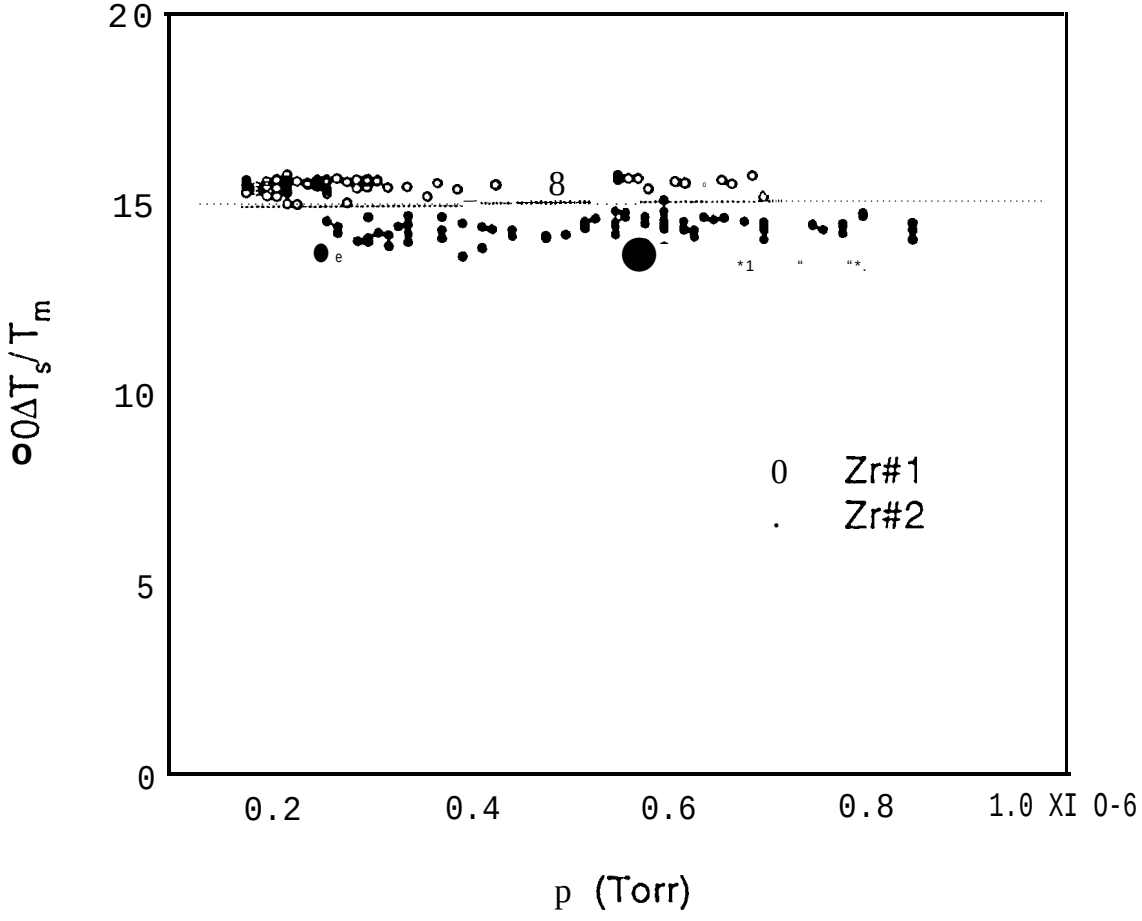

Fig. 3

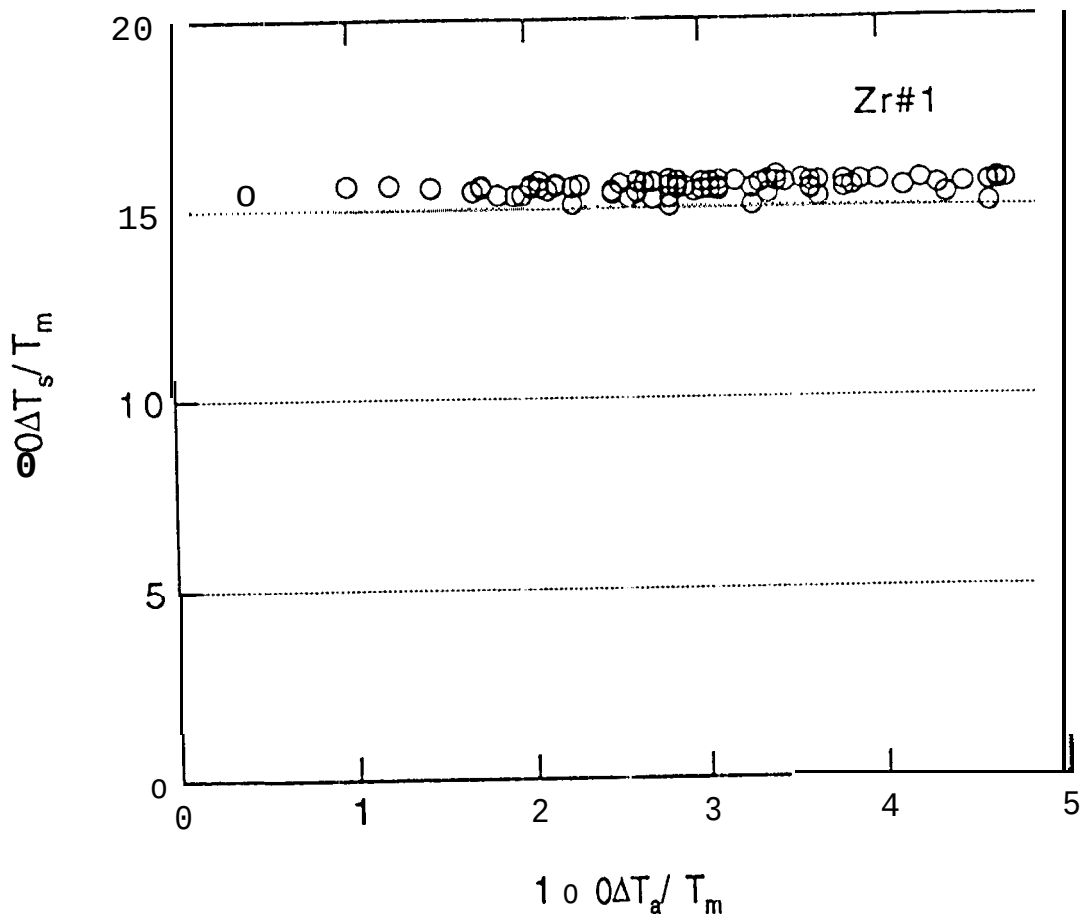

Fig. 4

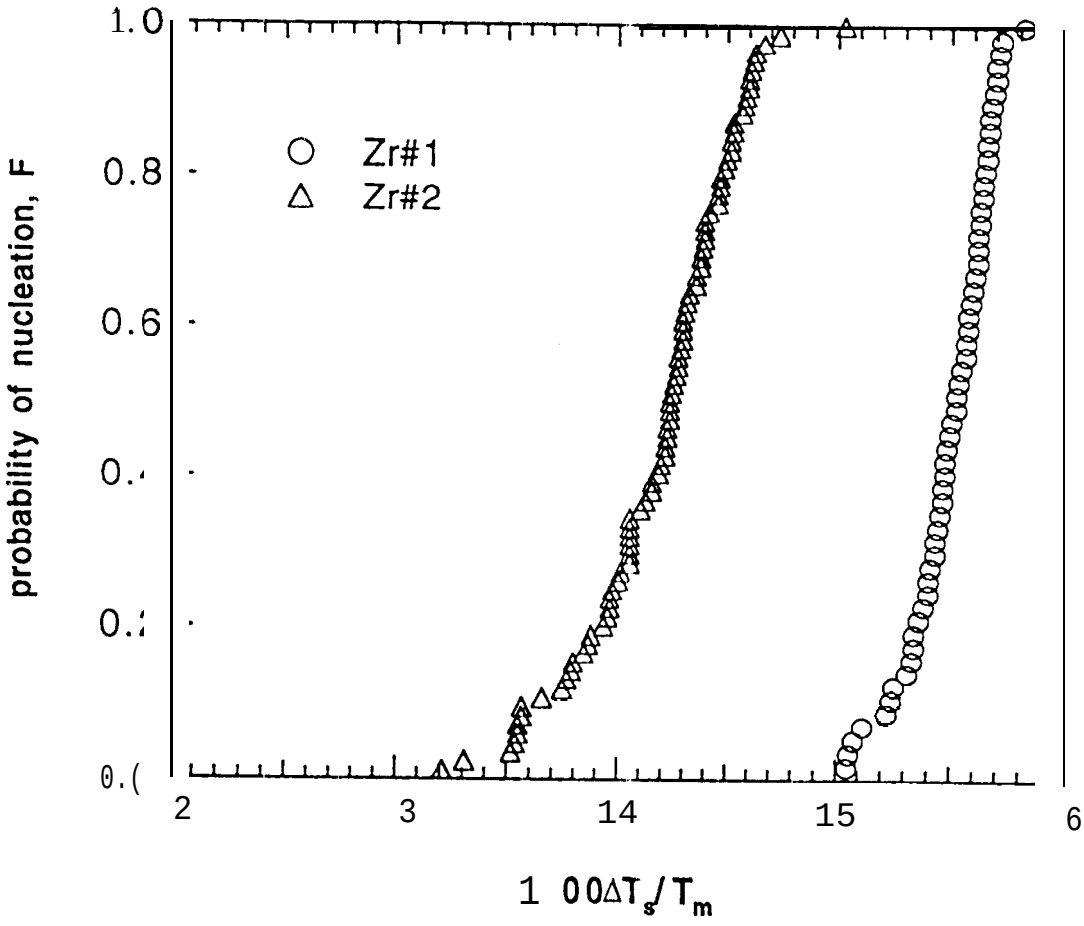
1.0
0.8
0.6
0.
0.
0.(
probability of nucleation, F
Zr#1
Zr#2
2
3
14
15
6
1 00ΔT_s/T_m

Fig. 5

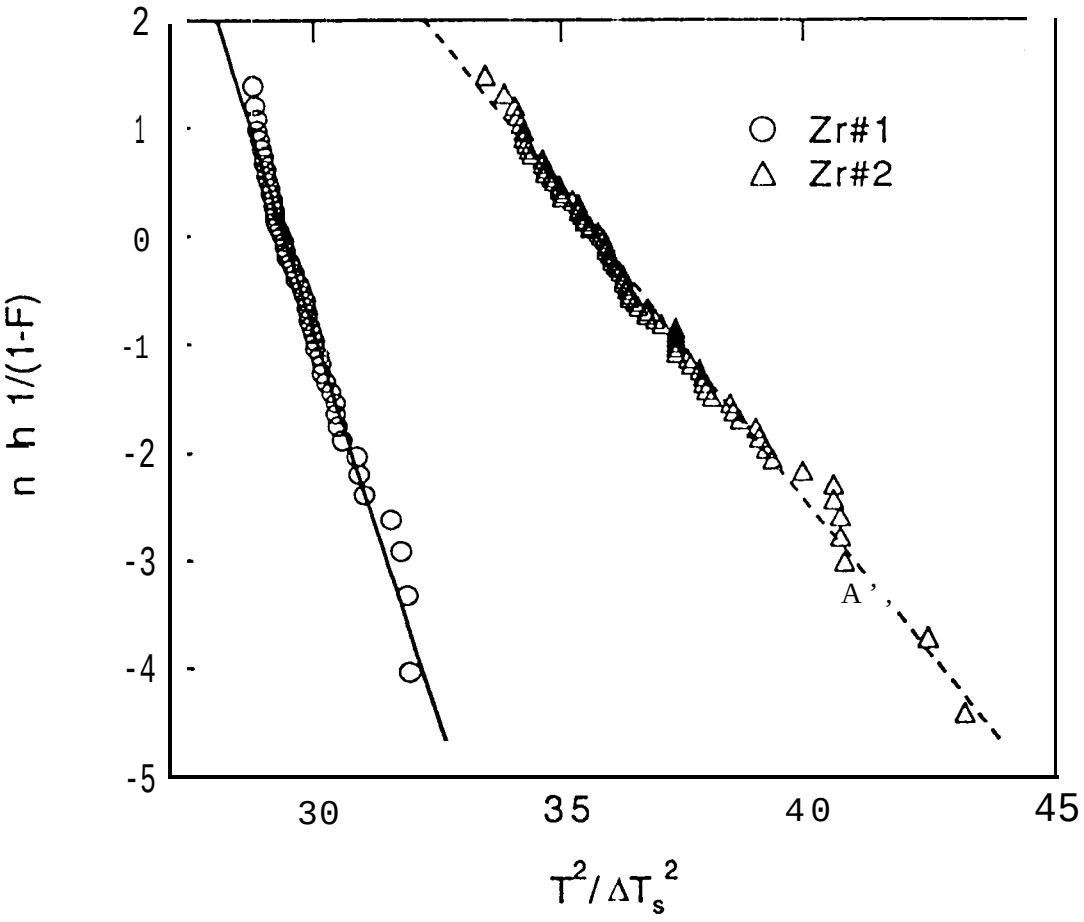

Fig. 6

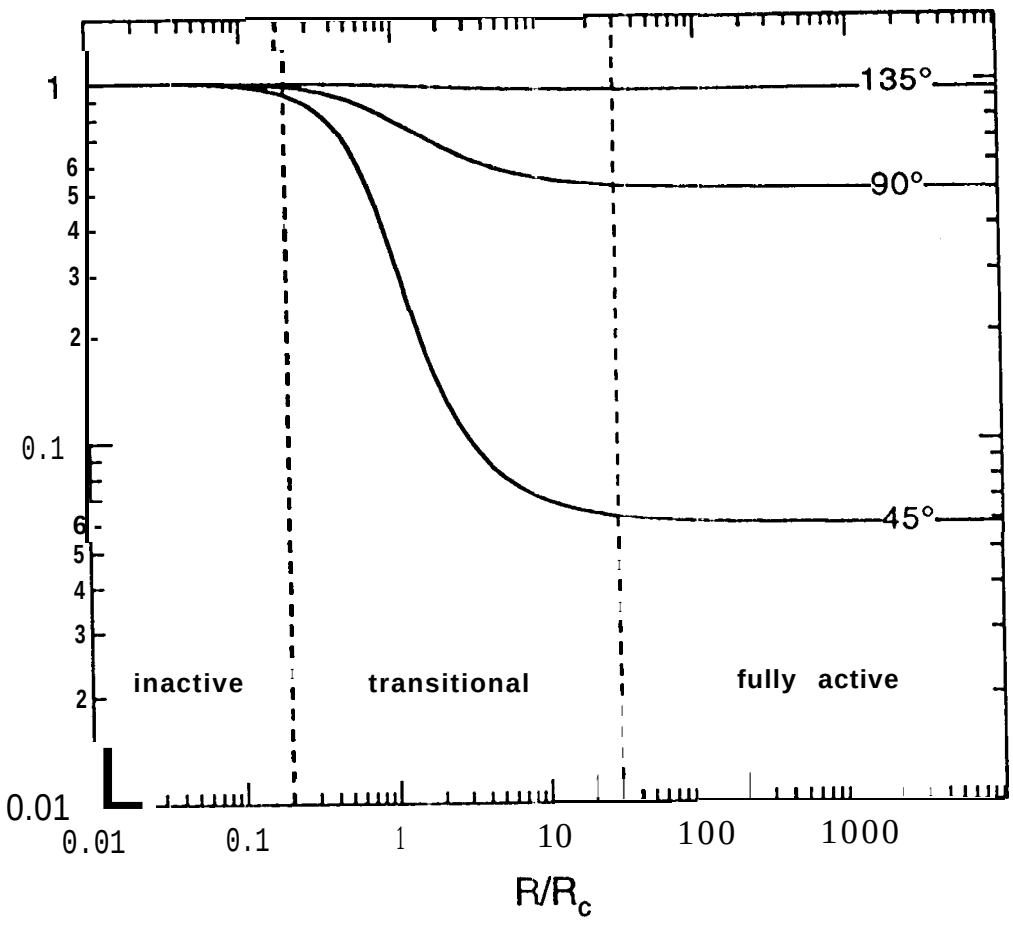
1
6
5
4
3
2
0.1
6
5
4
3
2
0.01
135°
90°
45°
inactive
transitional
fully active
0.01
0.1
1
10
100
1000
R/Rc

Fig. A1.